IOP Publishing Phys. Med. Biol. 70 (2025) 055013 https://doi.org/10.1088/1361-6560/adb679

Physics in Medicine & Biology

IPEM Institute of Physics and Engineering in Medicine

OPEN ACCESS

RECEIVED
19 December 2024

REVISED
2 February 2025

ACCEPTED FOR PUBLICATION
14 February 2025

PUBLISHED
25 February 2025

PAPER

Retrospective study on the resonance of thermoacoustic emissions and their possible biological implications in cats treated with electron FLASH beams

Julie Lascaud[1,*], **Martin Rädler**[1], **Carla Rohrer Bley**[2], **Marie-Catherine Vozenin**[3,4,5] and **Katia Parodi**[1]

[1] Department of Medical Physics, Ludwig-Maximilians-Universität München, Munich, Germany
[2] Clinic for Radiation Oncology & Medical Oncology, University Animal Hospital, Vetsuisse Faculty, University of Zurich, Zurich, Switzerland
[3] Sector of Radiobiology Applied to Radiotherapy, Radiation Oncology Department, Geneva University Hospital, Geneva, Switzerland
[4] LiRR—Laboratory of Innovation in Radiobiology Applied to Radiotherapy, Faculty of Medicine, University of Geneva, Geneva, Switzerland
[5] Laboratory of Radiation Oncology/Radiation Oncology Service, Department of Oncology, CHUV, Lausanne University Hospital and University of Lausanne, Lausanne, Switzerland
[*] Author to whom any correspondence should be addressed.

E-mail: j.lascaud@physik.uni-muenchen.de

Keywords: FLASH-RT, thermoacoustics, biology

Supplementary material for this article is available online

Abstract

Objective. Radiotherapy delivered at an ultra-high dose rate (UHDR) is a promising cancer treatment. In the last years, it has been shown to selectively reduce toxicity in healthy tissue by triggering the so-called FLASH effect achieved through specific temporal dose fractionation. However, the increase of the instantaneous dose rate results in the production of stronger thermoacoustic emissions for microsecond or shorter pulsed ionizing beams, which could potentially impact the treatment outcomes. Focusing on scenarios expected to create the highest acoustic intensities, the objectives of this work were to assess whether acoustic resonance can theoretically occur *in vivo* and how it could be mitigated in cases where it would influence the biological response. *Approach.* Thermoacoustic emissions were retrospectively simulated from post-treatment x-ray computed tomography scans of cats irradiated with a single high dose of electron FLASH to treat squamous carcinoma of the nasal planum. The peak dose, pressure intensity and location of the acoustic resonance were assessed for different beam positioning and reproduced for three animals. *Main results.* Irradiation of nasal planum in cats using a frontal electron beam results in pressure hot spots due to acoustic resonance that are observed in the vicinity of the rostral maxillary bone. The pressure distribution is mostly influenced by the anatomy (i.e. geometry and heterogeneous composition of the irradiated object), whereas its intensity largely depends on the irradiation setup. While further experimental investigation is needed to understand and mitigate potential associated risks, our results underline that acoustic phenomena so far neglected in conventional radiotherapy may need to be accounted for when using UHDR delivery. *Significance.* We show that specific irradiation scenarios can induce geometry-dependent thermoacoustic resonances *in vivo* which may be of sufficient magnitude to induce biological effects and impact the outcomes of FLASH radiotherapy.

1. Introduction

Radiotherapy treatments delivered at ultra-high dose rates (UHDR, larger than 40 Gy s^{-1}) are emerging as a new paradigm in cancer therapy. In recent years, the so-called FLASH effect, expected to be triggered in this regime for irradiation times lasting less than a few hundreds of milliseconds, has been shown to enlarge the

differential response between normal and cancer tissues in several animal models and with different radiation qualities (i.e. mostly with electrons and protons but also photons and heavy ions) (Favaudon *et al* 2014, Montay-Gruel *et al* 2017, Beyreuther *et al* 2019, Vozenin *et al* 2019). While the underlying mechanism(s) responsible for selectively reducing toxicity in healthy tissues remains to be elucidated (Limoli and Vozenin 2023), FLASH radiotherapy (FLASH-RT) is progressing toward the clinics. The feasibility of UHDR delivery was already demonstrated in a human patient treated with an electron beam in 2019 (Bourhis *et al* 2019) and confirmed in the last years with protons (Mascia *et al* 2023). However, the large doses, close to tissue tolerance limits, currently delivered in a single fraction raise safety concerns that needs to be meticulously assessed before translation to clinical practice.

Long-term follow-up pre-clinical studies have revealed the occurence of osteoradionecrosis (ORN) in the months after FLASH-RT when treating oral cavities with a high single dose ($\geqslant$30 Gy). First noticed in three out of seven cats treated for squamous cell carcinoma of the nasal planum at the Lausanne University Hospital (Lausanne, Switzerland) (Rohrer Bley *et al* 2022), the observation was confirmed in dogs (four out of six animals with malignant tumors of the oral cavity) at the University Hospital for Companion Animals (University of Copenhagen, Denmark) (Børresen *et al* 2023). A more recent study showed that ONR is not observed for dogs with diverse non-oral tumors treated with a single electron FLASH-RT fraction of up to 35 Gy (Gjaldbæk *et al* 2024). Hence, the ORN are attributed to dose hot spots caused by the complex tissue structure in the nasal cavity, resulting in dose locally exceeding the tissue tolerance limit. In the present study, we assess whether this distinct morphological characteristic could also be favorable to resonance of thermoacoustic emissions produced by pulsed ionizing beams, which could presumably impact the treatment outcomes.

Primary (or secondary for high-energy photons) charged particles lose their energy when traversing the irradiated medium. The dominant part of this energy loss is converted to heat. It leads to a high temperature increase in the surrounding of each particle track, expected to reach a few hundreds for electrons (Norman 1967) and up to a few thousands of Kelvin for heavy ions (Toulemonde *et al* 2009) at the (sub-)nanometer scale. Consistent warming up over the region covered by the ionizing beam results in thermal expansion and acoustic emission when heated on a time scale short enough to neglect thermal diffusion within the volume of interest (i.e. thermal confinement) (Baily 1992). The strength of this pressure wavefront is maximal when the ionizing pulse is shorter than the acoustic propagation time across the heated region (i.e. stress confinement, typically up to a few microseconds for centimeter-size clinical beams). Under these conditions and for a given temporal profile of the ionizing source, the pressure generated varies linearly with the instantaneous dose rate and the medium properties (e.g. density and energy-to-pressure conversion efficiency defined by the Grüneisen parameter). To date, ionizing radiation-induced acoustics has been mainly investigated for the monitoring of pulsed beams in radiotherapy (Sulak *et al* 1979, Mascarenhas *et al* 1984), with limited progress due to the challenging detection of the low-frequency (up to a few hundred kHz) and weak pressure (usually below 100 mPa) signals generated in conventional radiotherapy (Hickling *et al* 2018). The much higher instantaneous dose rates used in FLASH-RT provide ideal conditions, which have generated renewed interest and fostered new technical developments in the last years (Oraiqat *et al* 2020, Bjegovic *et al* 2024).

Several studies have started investigating the propagation and detection of thermoacoustic emissions *in vivo* to infer information on the impinging dose (Lehrack *et al* 2017, Forghani *et al* 2020, Samant *et al* 2022). Nevertheless, little is known on their possible contribution to the biological response in radiotherapy. Therapeutic ultrasound produced by an external source (i.e. ultrasound transducer positioned on the patient's skin) has been used in therapy for many years to induce diverse biological responses depending on the intensity and frequency of the acoustic emissions. Low- and high-intensity ultrasound is notably known to favor species diffusion (Mortimer and Dyson 1988), stimulate cell and protein synthesis (Webster *et al* 1978), or regulate inflammatory response (Doan *et al* 1999). *In vivo*, acoustic cavitation of bubbles, injected or naturally present in tissues, can cause cell membrane permeabilization (Sundaram *et al* 2003) and mechanical disruption (Lentacker *et al* 2014). *In vitro* studies have revealed that ultrasound cause more damage to cancer cells compared to their healthy counterparts for the investigated cell lines, which was further enhanced in the presence of acoustic standing waves (i.e. spatial resonance)(Mittelstein *et al* 2020). Combined with radiotherapy, ultrasound-triggered destruction of injected microbubbles performed in the hours before or after irradiation was also shown to sensitize cancerous cells to radiation (Lacerda *et al* 2021). Hence, thermoacoustic emissions of sufficiently high amplitude could trigger several biological processes, either positively or negatively influencing the outcomes of FLASH treatments depending on their intensity. While a biological contribution seems irrelevant in conventional therapy in view of the weak pressure waves generated, the orders of magnitude increase expected in FLASH-RT motivates further investigation of this mechanical effects.

In a first dedicated in-silico investigation we showed that thermoacoustic emissions produced in scenarios similar to an early electron FLASH-RT study with mice could reach an amplitude sufficient to induce acoustic cavitation (i.e. oscillation and possible collapse of gas bubbles) (Lascaud and Parodi 2023). This preliminary simulation-based investigation conducted using simple phantoms highlighted a major impact of the geometry on the peak pressure. Particularly, if the irradiated volume is smaller than the beam diameter or in the presence of strong heterogeneities (e.g. air cavities or bones), multiple reflections within the irradiated object may interfere constructively in some regions. The acoustic resonance results in a local enhancement of the pressure amplitude, where the biological response is more likely to be altered. Building upon our previous study, this work assesses whether acoustic resonance can theoretically occur *in vivo*. We hereby focus on scenarios where the pressure could reach the highest peak amplitudes. We hypothesize that in these particular cases, the biological response could be locally modified by acoustic effects. The impact of the thermoacoustic emissions could, however, be mitigated by slightly adjusting the irradiation parameters to dampen their resonance. To assess this, we retrospectively investigated thermoacoustic emissions produced during electron FLASH-RT delivery in the cats who developed post-irradiation ORN (Rohrer Bley *et al* 2022). In fact, the microsecond-short pulse of electrons, delivered by the linear accelerator at a remarkably high instantaneous dose rate of 5.6×10^6 Gy s^{-1}, combined with the heterogeneities of the nasal cavity, creates a scenario particularly favorable for the resonance of already strong acoustic emissions. The influence of the irradiation geometry on the resonance is also evaluated for several beam positions.

2. Material and methods

2.1. Cat imaging and contouring

Thermoacoustic emissions and their propagation *in vivo* were assessed from the post-treatment x-ray computed tomography (CT) scans, only available for three cats (cat1 without ORN, cat2 and cat3 both with ORN) out of the seven included in the original study. These follow-up images were acquired in pre- and post-contrast mode on a 16 multidetector CT unit (Brilliance CT 16-slice, Philips Health Care Ltd Best, Netherlands). For contouring, 2 mm reconstructed slice thickness and bone window were used. The gross tumor volume (GTV) was defined as the macroscopically visible part of the lesion on the planum nasale of the cats and a clinical target volume, accounting for sub-clinical microscopic disease extension of 5 mm (presumed local infiltration) was included. The contours of ORN were delineated with Eclipse External Beam Planning system version 15.1.51 (Varian Oncology Systems, Palo Alto, USA).

2.2. Electron beam model

The dose deposited by the electron beam was calculated using the FLUKA Monte Carlo code (PRECISIOn defaults, version 2023.3.2) (Ferrari *et al* 2005, Böhlen *et al* 2014). The beam parameters were tuned to reproduce the same dosimetry characteristics (i.e. depth dose and lateral profiles) as measured with EBT-XD films during the irradiation of a phantom made of water equivalent material (Rohrer Bley *et al* 2022). For the simulation, the solid phantom was replaced by water with a density of 1000 kg m^{-3} and an ionization potential of 78 eV. Similarly to the experiments, the 6 MeV electron beam with a diameter of 2.6 cm goes through a 31.8 cm-long tubular PMMA applicator. A beam divergence of 200 mrad with a Gaussian distribution was assumed to better reproduce the peak-to-entrance dose ratio and match the overall shape of the lateral profiles. The resulting dose profiles in water are depicted in figure S1 of the supporting material.

2.3. Simulation setup and workflow

The simulation framework is similar to our previous work (Lascaud and Parodi 2023) and summarized in figure 1. The CT scans were up-sampled using linear interpolation (TorchIO version 0.18.91) to reduce the grid spacing down to 0.5 mm isotropically, as required for the acoustic simulations. The same parameters and setup were used to model the 6 MeV electron beam (see figure 1(b)) in all cases. A 250 μm water layer was positioned directly after the applicator (green layer in figure 1(b)) to model the EBT-XD film used during the experiments. The mean dose in the entrance in Gy/primary (figure 1(a)) was used to determine the number of electrons required to match the experimental dose of about 10 Gy per pulse (total dose of 30 Gy delivered in 3 pulses over 20 ms). The exact value was adapted for each cat based on data available from the film measurements. Similarly to the experiments, the electron beam and applicator were first centered to the targeted volume (GTV center of mass positioned at x_0 and y_0, see figure 1(h)). Note that, in all cases thereafter, the doses reported in Gy or Gy/primary always refer to the dose to medium. The simulations were repeated for different beam positions to assess the impact of the irradiation geometry on the acoustic resonance. In total, 8 additional positions were investigated and obtained by shifting the beam by $\pm$5 mm on the x- and y-axes (figure 1(h)).

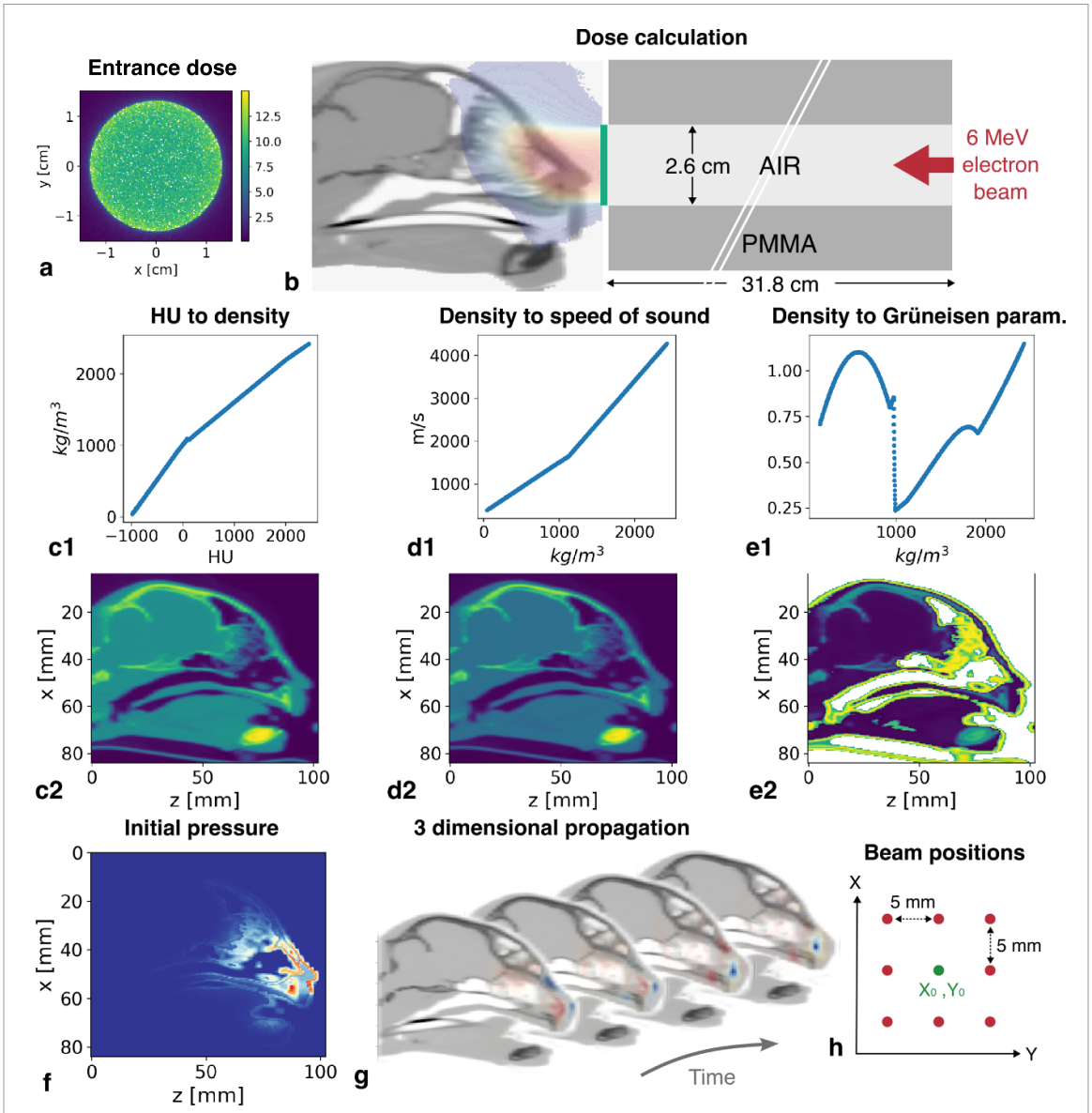

Figure 1. Simulation workflow. (a) Two-dimensional dose in the water slab placed after the applicator. (b) Setup used for the dose calculation in FLUKA. The green layer on the left of the PMMA block indicated the water layer location. The red arrow shows the beam starting position. (c1) HU to density conversion curve and (c2) exemplary two-dimensional density map. (d1) Density to speed of sound conversion curve and (d2) exemplary two-dimensional speed of sound map. (e1) Density to Grüneisen parameter conversion curve and (e2) exemplary two-dimensional Grüneisen parameter map. (f) Exemplary initial pressure map in the same slice as (c2) to (e2). (g) Snapshots of the pressure wavefront propagation during the first 10 μs. (h) Nominal position of the electron beam (x_0, y_0) and relative positions investigated. For all the colormaps, lowest values in blue and highest values in yellow (a), (c2), (d2), (e2) or red (b), (f), (g).

The initial pressure derived from the dose distribution was propagated in three dimensions using a k-space pseudospectral method (GPU implementation of the *k*-Wave toolbox, version 1.3 (Treeby and Cox 2010)). The spatially varying density $\rho(\boldsymbol{r})$ was derived from the x-ray Hounsfield units using the conversion table available in FLUKA (figures 1(c1) and (c2)). The same segmentation was used to define the medium density in *k*-Wave. The speed of sound and Grüneisen parameter $\Gamma(\boldsymbol{r})$ were obtained from the medium density (figures 1(d1), (d2) and (e1), (e2), respectively) as previously proposed (Yu *et al* 2019). Attenuation in the medium was neglected given the low-frequency of the expected pressure wavefront (much below the MHz). The simulated dose $D(\boldsymbol{r})$ was converted to an initial pressure ($P_0(\boldsymbol{r})$ in figure 1(f)) as defined in equation (1),

$$P_0(\boldsymbol{r}) = \Gamma(\boldsymbol{r}) \times \rho(\boldsymbol{r}) \times D(\boldsymbol{r}). \quad (1)$$

The simulations were performed for a delta-spike temporal excitation (i.e. set as *initial value problem* in *k*-Wave). The time step was defined to have a Courant–Friedrichs–Lewy number (ratio of the distance traveled by the wave in one time step to the grid spacing) equals to 0.2, ensuring the simulation stability and

accuracy. Spurious reflections were prevented by keeping the perfectly matched layers as implemented by default in *k*-Wave. The evolution of the pressure over time was scored on a uniform three dimensional grid (1 mm spacing) covering the nasal cavity, allowing for the reconstruction of the pressure wavefront in time and space after propagation (see snapshots in figure 1(g)). The simulated time series were convolved with a 1.8 μs rectangular pulse, modeling the shape of the actual electron pulse. The pulse amplitude was normalized such that its sum equals the number of electrons defined from the simulated entrance dose. Details of the convolution and normalization are illustrated in the supplementary data.

2.4. Data analysis

For each position on the pressure scoring grid, the peak negative pressure P_{neg} and peak frequency were extracted. For the latter, the signals in the time domain were zero-padded before calculating the fast Fourier transform to increase the frequency resolution to 1 kHz. The pressure cavitation thresholds (P_{cav} in MPa) at a given frequency (f in MHz) were estimated for blood using the empirical approach proposed by Apfel and Holland (1991) (equation (2)) where a and c are two empirical constants, equal to 1.67 and 0.13, respectively,

$$P_{\text{cav}} = \sqrt[a]{c \times f}. \tag{2}$$

The similarity between the spatial locations of the peak negative pressure for different beam positions was quantified by calculating the overlap coefficient, defined in equation (3) as:

$$\text{overlap}\left(P_{80(x_0,y_0)}, P_{80(x_n,y_n)}\right)[\%] = \frac{\left|P_{80(x_0,y_0)} \cap P_{80(x_n,y_n)}\right|}{\min\left(\left|P_{80(x_0,y_0)}\right|, \left|P_{80(x_n,y_n)}\right|\right)} \times 100 \tag{3}$$

where $P_{80(x_0,y_0)}$ and $P_{80(x_n,y_n)}$ are the volumes encompassing negative pressure superior to 80% of the maximum peak negative pressure (P_{max}) obtained at the nominal position of the electron beam ($x = x_0$ and $y = y_0$) and after shifting it, respectively.

3. Results

3.1. Assessment of the acoustic resonance *in vivo*

Figure 2 shows the dose (a)–(c), initial pressure distributions (d)–(f) and peak negative pressure map (g)–(i) for the animals without and with ORN, respectively. Similarly to previous retrospective dose calculation performed using a treatment planning system (Rohrer Bley *et al* 2022), hot spots of dose above 125% of the prescribed value are observed in bony regions (here peak dose of 14.4 Gy/pulse, 15.8 Gy/pulse and 14.7 Gy/pulse for cat1, cat2 and cat3, respectively). The pressure increase consecutive to the brief medium heating depends on the dose deposited, the medium density and tissue specific efficiency of the energy-to-pressure conversion (i.e. Grüneisen parameter that is higher in fatty layers and bones than in soft tissues or air). This is reflected in the initial pressure distribution which mostly follows the *in vivo* dose. Additional high values are obtained in the bony regions and on the skin, resulting in a maximum initial pressure of about 10 kPa.

The subsequent propagation of the initial pressure in tissues is constrained by the head morphology. The strong acoustic impedance mismatch at the interfaces with air cavities and bones causes the wavefront to entail multiple reflections. It leads to a pressure enhancement (peak negative pressure of 14.3 kPa, 16.4 kPa and 12.5 kPa for cat1, cat2 and cat3, respectively), with pressure hot spots observed in the vicinity of the rostral maxillary bone for the three cats. Taking into account tissue specific density and speed of sound, this corresponds to a maximum pressure intensity of 20 mW cm^{-2} 32 mW cm^{-2} and 224 mW cm^{-2} for cat1, cat2 and cat3, respectively (see figure S3 of the supporting material) in the area where the pressure hot spots are observed. For all the investigated scenarios, P_{neg} remains below the cavitation threshold (P_{max} lower than 30% of the pressure cavitation threshold) identified by Apfel and Holland for micrometer-sized gas-filled bubbles (see the normalized P_{neg} maps in figure S4 of the supporting material).

3.2. Influence of the irradiation setup on the *in vivo* resonance

The peak negative pressure distribution is illustratively presented in figures 3(a)–(c) for electron beams at different lateral positions (±5 mm relative to the target center along the y-axis as defined in figure 1(h)) for the cat without ORN (cat1). Details of the nine investigated positions for the three animals are given in the supporting materials (figures S5–S7). Moving the electron beam with regard to the target results in a variation of the absolute peak pressure value and slight modification of the hot spot volume. However, for all the investigated setups, the location of the pressure hot spot is preserved and consistently observed close to the palate rostral part. This is depicted by the mean overlap coefficient between $P_{80\%}$ at initial position and

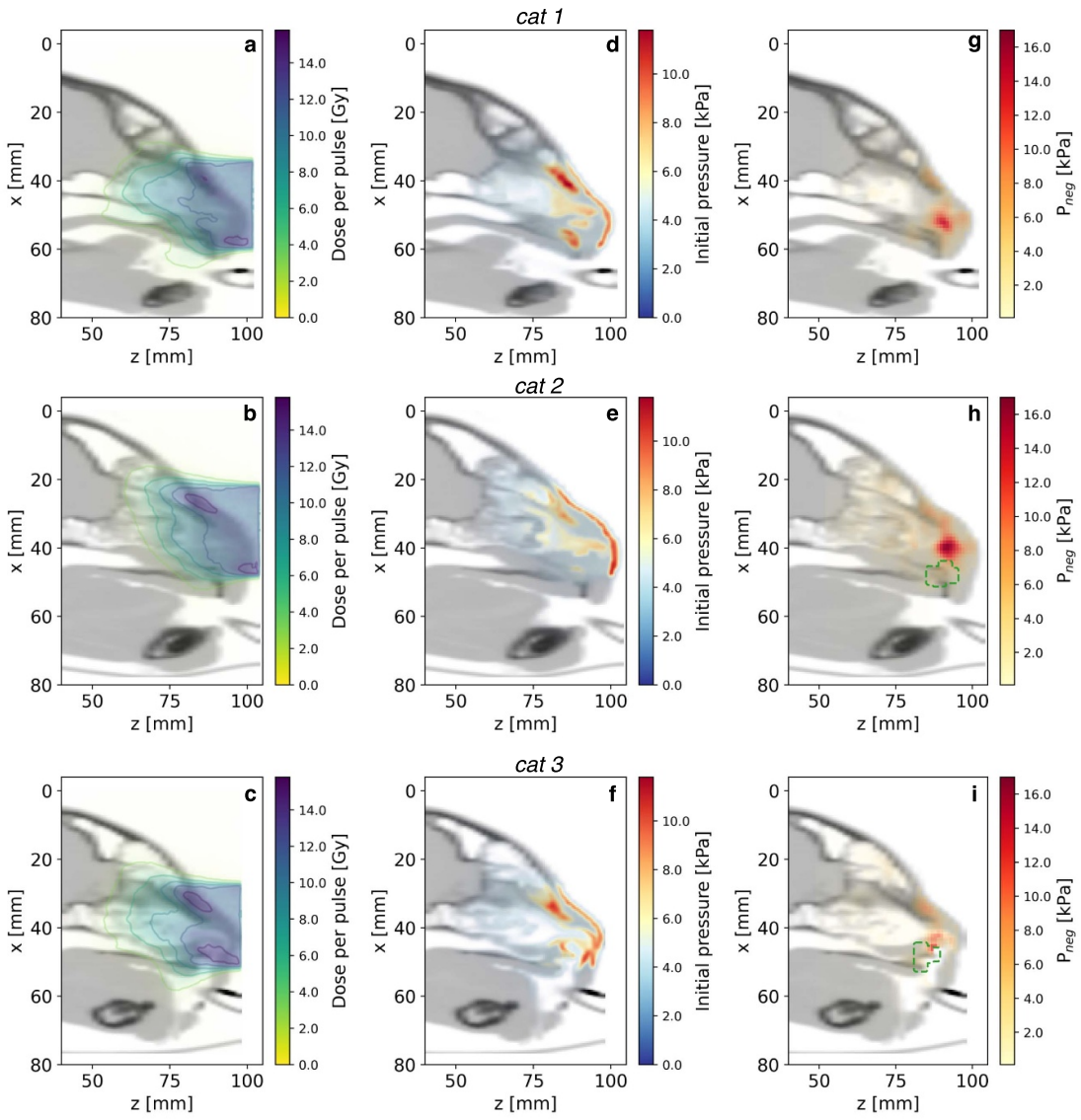

Figure 2. Dose and pressure distribution in cats without (first row) and with osteoradionecrosis (ORN) post-irradiation (two last rows) overlaid to corresponding CT scan in the sagittal plane with the electron beam centered to the targeted volume. (a)–(c) Dose per pulse (isocurves representing 25%, 50%, 75%, 100% and 125% of the prescribed dose), (d)–(f) initial pressure distribution (i.e. before acoustic propagation), and (g)–(i) negative peak pressure map. The green dashed lines show the ORN contour. All data showed in CT slice corresponding with the highest negative peak pressure.

$P_{80\%}$ for different beam offsets along x- and y-axes (overlap$(P_{80(x_0,y_0)}, P_{80(x_n,y_n)})$) equals to 68% with a standard deviation of 20% ($68\% \pm 20\%$) in all scenarios.

Figures 3(d)–(f) and (g)–(i) show the variation of the peak dose per pulse and corresponding peak negative pressure for the three cats at the different irradiation positions relative to the maximum value obtained when the beam is centered to the target. For the simulated geometries, the maximum dose is not considerably impacted by the beam position, changing only by up to 10% between the central beam position and after shifting it up to 5 mm (average value of the maximum dose and its standard deviation for each irradiation geometry of 15.1 ± 0.4 Gy/pulse, 15.4 ± 0.7 Gy/pulse and 14.8 ± 0.5 Gy/pulse for cat1, cat2 and cat3, respectively). At the opposite, the peak negative pressure, which varies by up to 110% in cat3 across the different beam locations (average maximum peak pressure and its standard deviation for each beam position of 15.9 ± 5.0 kPa, 15.8 ± 2.0 kPa and 16.9 ± 7.0 kPa for cat1, cat2 and cat3, respectively), widely depends on the irradiation setup. Dose and pressure variations are not directly correlated. A decrease of the dose does not necessary results in a pressure drop and reversely (e.g. $x = -5$ cm; -5 cm in cat1). Moreover, the position where the highest dose increase is observed does not correspond with the location of the highest peak pressure rise (e.g. highest dose at [5 cm; -5 cm] and highest pressure at [5 cm; 0 cm] for cat3).

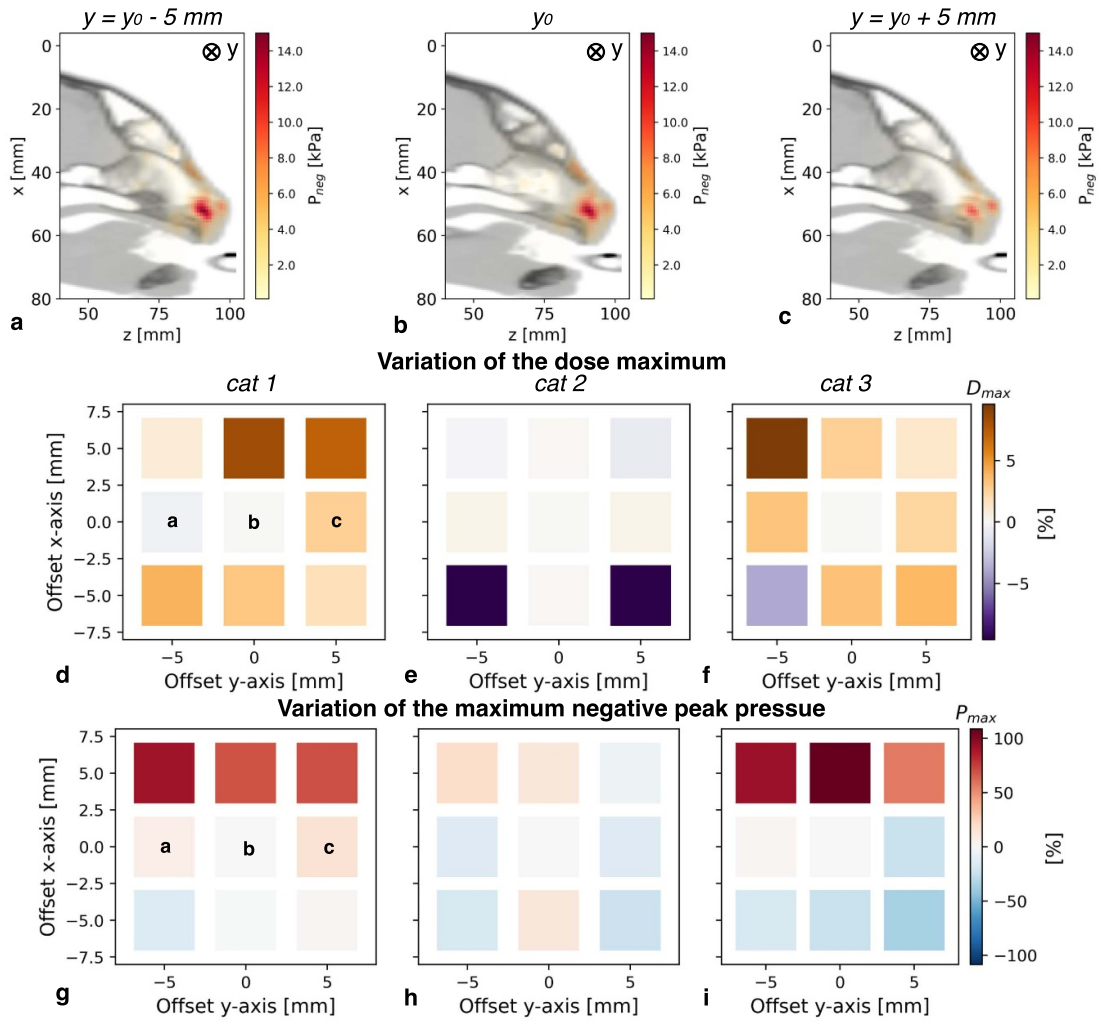

Figure 3. Peak dose and pressure depending on the beam position. Exemplary maps of the negative peak pressure for beam offset by (a) −5 mm and (c) 5 mm along the *y*-axis relative to (b) initial position centered to the target in cat without necrosis. Variation of the peak dose per pulse (d)–(f) and negative peak pressure (g)–(i) relative to the peak values at the initial beam position for cat1, cat2 and cat3, respectively.

4. Discussion

4.1. Study limitations

Our results show that irradiation of nasal planum in cats using a frontal electron beam can induce acoustic resonance *in vivo* with pressure hot spots found in the vicinity of the rostral maxillary bone. While the location of the points of maximum pressure does not considerably vary with the beam position, the spot intensity is largely impacted. Here, the pressures do not exceed cavitation thresholds previously identified for media containing microbubbles ($P_{\max}/P_{\text{cav}} = 28\% \pm 10\%$). However, our analysis was conducted from post-treatment images that include morphological changes (i.e. alteration of the bony structure in the months following the irradiation and animal repositioning). The medium properties and, in particular, the Grüneisen parameter are also not well-known *in vivo*. Both changes in the cat anatomy and inaccurate medium properties could lead to large over- or under-estimation of the peak pressure. Based on our results and previous work (Lascaud and Parodi 2023), this could be expected to vary by up to one order of magnitude. The present results are not sufficient to draw a clear conclusion on possible biological effects induced by acoustic resonance in FLASH-RT. Nevertheless, the pressure intensity reported and their large variability, highlight the need for further experimental investigations of these acoustic phenomena.

4.2. Irradiation scenarios favorable to acoustic resonances

Not all irradiation scenarios are prone to acoustic resonance of intensity sufficiently high to be biologically relevant. Resonance is more likely to occur in strongly heterogeneous tissues, such as the oral or the thoracic cavities. The duration of the macroscopic ionizing pulse should also match the frequency dictated by the

initial pressure distribution. In clinical applications, this is typically obtained with pulses of up to a few microseconds, independently of the radiation quality (i.e. electrons or ions). Note, the pressure is expected to fade out after a few hundreds of microseconds (Lascaud and Parodi 2023). Therefore, pulses delivered at a repetition rate below the kHz can be seen as independent from each other. Furthermore, continuous variation in beam intensity with nanosecond periodicity cannot be resolved acoustically. Hence, the microscopic pulsing structure that may be inhered from the acceleration process is not known to impact the thermoacoustic emissions. Considering machines available or those foreseen to support FLASH-RT, electron beams delivered by microsecond pulses with a repetition rate of a few hundreds of Hz at linear accelerators or emerging very high energy electrons will give the strongest emissions. For these modalities, adjusting the irradiation setup (e.g. ionizing beam position and angle) might be required to minimize the pressure hot spot intensity. Protons or heavier ions typically delivered quasi-continuously for a few milliseconds by clinical isochronous cyclotron or synchrotron accelerators at a much lower instantaneous dose rates are of lower concern, while the pressure at synchrocyclotrons should be assessed in FLASH conditions.

4.3. Possible biological impact of thermoacoustic emissions

Although comprehensive experimental investigations of the physics and biology potentially involved would be required to discuss a putative acoustics modulation of FLASH-RT outcomes, the approximate characteristics of the thermoacoustic emissions derived from this study allow to hypothesize a few phenomena by which this could occur. The few tens of kPa reported here, corresponding to acoustic intensity in the order of 10 to 100 mW cm^{-2}, is sufficient to enhance the diffusion of chemical species (Mortimer and Dyson 1988). Therefore, acoustic waves could locally alter the post-ionization chemistry, those precisely known to be partially involved in the FLASH effect. The low intensity ultrasound could also modulate the inflammatory response and favor rapid recovery. While in this pressure range the additional acoustic effects are more likely to lower FLASH-RT toxicity in soft tissues, they might result in side effects in the presence of micrometer sized gas bubbles. In theory, the nucleation of bubbles in pure degassed water at room temperature (here assumed as a surrogate of biological materials) requires an acoustic pressure of about 100 MPa (Apfel 1997), way above the peak values reported here. However, this threshold is known to reduce when sonification is performed during irradiation, as first demonstrated by Finch with a pulsed neutron beam (Finch 1964). The phenomenon is assumed to be caused by the formation of (sub-)micrometer gas bubbles resulting from the local heating around the particle track (thermal spike). The size of the gas pockets formed and their stability over time vary depending on the energy deposited along the particle track (linear energy transfer, LET) and the fluid degree of superheating that describes the liquid temperature above its boiling point. A fluid with a higher degree of superheat requires less input energy to vaporize a certain volume. Hence, the higher the degree of superheat is, the larger the bubbles will be for a given energy loss. Such a gas cavity could be expected to be nanometer-sized (Norman and Spiegler 1963) with a lifetime of up to a few microseconds (Ljunggren and Eriksson 1997) for individual tracks within low LET electron beams in the considered energy range. However, at UHDR used in FLASH-RT, the inter-track distance is considerably reduced. For the present 6 MeV electron beam, the average inter-track distance at UHDR is estimated to 8 nm from Monte Carlo simulations (see supporting material). In contrast, it is about 100 μm at a conventional dose rate. Because of the close vicinity of the particle track, cavities formed in the still-warm tail of a previous particle may nucleate in superheated water, resulting in larger and more stable bubbles (Ghormley 1958). They are also more likely to collide during their expansion or interact with shock waves emitted from neighboring tracks, leading to further oscillations or collapse within the bubble cloud and formation of larger bubbles (Abolfath *et al* 2024). It is worth notifying that, these nano-acoustic inter-track effects, presumably observed in FLASH-RT for any beam quality delivered at sufficiently high (instantaneous) dose rates, would strongly depend on the mechanical properties of the medium. As a consequence, it should vary for different tissue types which could in part explain the selectivity between normal and cancerous tissues.

5. Conclusions

This work assessed thermoacoustic emissions in cats treated with an electron FLASH beam. We showed that irradiation of nasal planum in cats using a frontal electron beam can induce acoustic resonance near the rostral maxillary bone, with acoustic intensity widely dependent on the irradiation setup. Further experimental investigations are required to better evaluate the strength of the pressure produced in FLASH-RT and suggested acoustic cavitation of gas bubbles formed along the ionizing beam at UHDR. However, our results underline that acoustic phenomena so far neglected in conventional therapy may need to be accounted for when using UHDR delivery, notably when irradiating heterogeneous media with microsecond-pulsed ionizing beams.

Data availability statement

The data cannot be made publicly available upon publication because they are not available in a format that is sufficiently accessible or reusable by other researchers. The data that support the findings of this study are available upon reasonable request from the authors.

Acknowledgments

This study was supported by LMUexcellent, funded by the Federal Ministry of Education and Research (BMBF) and the Free State of Bavaria under the Excellence Strategy of the Federal Government and the Länder. The initial study with animals was supported by the Krebsliga (KFS-4438-02-2018).

ORCID iDs

Julie Lascaud https://orcid.org/0000-0002-7649-6909
Martin Rädler https://orcid.org/0000-0003-3313-2993
Carla Rohrer Bley https://orcid.org/0000-0002-5733-2722
Marie-Catherine Vozenin https://orcid.org/0000-0002-2109-8073
Katia Parodi https://orcid.org/0000-0001-7779-6690

References

Abolfath R, Afshordi N, Rahvar S, van Duin A C T, Rädler M, Taleei R, Parodi K, Lascaud J and Mohan R 2024 A molecular dynamics simulation framework for investigating ionizing radiation-induced nano-bubble interactions at ultra-high dose rates *Eur. Phys. J.* D **78** 141

Apfel R E 1997 Sonic effervescence: a tutorial on acoustic cavitation *J. Acoust. Soc. Am.* **101** 1227–37

Apfel R E and Holland C K 1991 Gauging the likelihood of cavitation from short-pulse, low-duty cycle diagnostic ultrasound *Ultrasound Med. Biol.* **17** 179–85

Baily N A 1992 A review of the processes by which ultrasound is generated through the interaction of ionizing radiation and irradiated materials: some possible applications *Med. Phys.* **19** 525–32

Beyreuther E, Brand M, Hans S, Hideghéty K, Karsch L, Leßmann E, Schürer M, Szabó E R and Pawelke J 2019 Feasibility of proton FLASH effect tested by zebrafish embryo irradiation *Radiother. Oncol.* **139** 46–50

Bjegovic K *et al* 2024 4d *in vivo* dosimetry for a FLASH electron beam using radiation-induced acoustic imaging *Phys. Med. Biol.* **69** 115053

Böhlen T, Cerutti F, Chin M, Fassó A, Ferrari A, Ortega P, Mairani A, Sala P, Smirnov G and Vlachoudis V 2014 The FLUKA code: developments and challenges for high energy and medical applications *Nucl. Data Sheets* **120** 211–4

Børresen B, Arendt M L, Konradsson E, Bastholm Jensen K, Bäck S, Munck af Rosenschöld P, Ceberg C and Petersson K 2023 Evaluation of single-fraction high dose FLASH radiotherapy in a cohort of canine oral cancer patients *Front. Oncol.* **13** 1256760

Bourhis J *et al* 2019 Treatment of a first patient with FLASH-radiotherapy *Radiother. Oncol.* **139** 18–22

Doan N, Reher P, Meghji S and Harris M 1999 In vitro effects of therapeutic ultrasound on cell proliferation, protein synthesis and cytokine production by human fibroblasts, osteoblasts and monocytes *J. Oral Maxillofac. Surg.* **57** 409–19

Favaudon V *et al* 2014 Ultrahigh dose-rate FLASH irradiation increases the differential response between normal and tumor tissue in mice *Sci. Trans. Med.* **6** 245ra93–245ra93

Ferrari A, Sala P R, Fassó A and Ranft J 2005 FLUKA: a multi-particle transport code *Report* CERN-2005-10 INFN/TC 05/11, SLAC-R-773 (OSTI Information Bridge Server, CERN Document Server)

Finch R 1964 Influence of radiation on the cavitation threshold of degassed water *J. Acoust. Soc. Am.* **36** 2287–92

Forghani F, Mahl A, Patton T J, Jones B L, Borden M A, Westerly D C, Altunbas C, Miften M and Thomas D H 2020 Simulation of x-ray-induced acoustic imaging for absolute dosimetry: accuracy of image reconstruction methods *Med. Phys.* **47** 1280–90

Ghormley J A 1958 Nucleation of bubbles in superheated aqueous solutions by fast particles *J. Nucl. Energy* **6** 300–2

Gjaldbæk B W, Arendt M L, Konradsson E, Jensen K B, Bäck S, af Rosenschöld P M, Ceberg C, Petersson K and Børresen B 2024 Long-term toxicity and efficacy of FLASH radiotherapy in dogs with superficial malignant tumors *Front. Oncol.* **14** 1425240

Hickling S, Xiang L, Jones K C, Parodi K, Assmann W, Avery S, Hobson M and El Naqa I 2018 Ionizing radiation-induced acoustics for radiotherapy and diagnostic radiology applications *Med. Phys.* **45** e707–21

Lacerda Q, Tantawi M, Leeper D B, Wheatley M A and Eisenbrey J R 2021 Emerging applications of ultrasound-contrast agents in radiation therapy *Ultrasound Med. Biol.* **47** 1465–74

Lascaud J and Parodi K 2023 On the potential biological impact of radiation-induced acoustic emissions during ultra-high dose rate electron radiotherapy: a preliminary study *Phys. Med. Biol.* **68** 05LT01

Lehrack S *et al* 2017 Submillimeter ionoacoustic range determination for protons in water at a clinical synchrocyclotron *Phys. Med. Biol.* **62** L20

Lentacker I, De Cock I, Deckers R, De Smedt S and Moonen C 2014 Understanding ultrasound induced sonoporation: definitions and underlying mechanisms *Adv. Drug Deliv. Rev.* **72** 49–64

Limoli C L and Vozenin M-C 2023 Reinventing radiobiology in the light of FLASH radiotherapy *Annu. Rev. Cancer Biol.* **7** 1–21

Ljunggren S and Eriksson J C 1997 The lifetime of a colloid-sized gas bubble in water and the cause of the hydrophobic attraction *Colloids Surf.* A **129** 151–5

Mascarenhas S, Vargas H and Cesar C 1984 A photoacoustical radiation dosimeter *Med. Phys.* **11** 73–74

Mascia A E *et al* 2023 Proton FLASH radiotherapy for the treatment of symptomatic bone metastases: the FAST-01 nonrandomized trial *JAMA Oncol.* **9** 62

Mittelstein D R, Ye J, Schibber E F, Roychoudhury A, Martinez L T, Fekrazad M H, Ortiz M, Lee P P, Shapiro M G and Gharib M 2020 Selective ablation of cancer cells with low intensity pulsed ultrasound *Appl. Phys. Lett.* **116** 013701

Montay-Gruel P et al 2017 Irradiation in a FLASH: unique sparing of memory in mice after whole brain irradiation with dose rates above 100 Gy/s *Radiother. Oncol.* **124** 365–9
Mortimer A and Dyson M 1988 The effect of therapeutic ultrasound on calcium uptake in fibroblasts *Ultrasound Med. Biol.* **14** 499–506
Norman A 1967 Thermal spike effects in heavy-ion tracks *Radiat. Res. Suppl.* **7** 33
Norman A and Spiegler P 1963 Radiation nucleation of bubbles in water *Nucl. Sci. Eng.* **16** 213–7
Oraiqat I, Zhang W, Litzenberg D, Lam K, Ba Sunbul N, Moran J, Cuneo K, Carson P, Wang X and El Naqa I 2020 An ionizing radiation acoustic imaging (iRAI) technique for real-time dosimetric measurements for FLASH radiotherapy *Med. Phys.* **47** 5090–101
Rohrer Bley C et al 2022 Dose- and volume-limiting late toxicity of FLASH radiotherapy in cats with squamous cell carcinoma of the nasal planum and in mini pigs *Clin. Cancer Res.* **28** 3814–23
Samant P, Trevisi L M, Chen Y, Zwart T and Xiang L 2022 3-D protoacoustic imaging through a planar ultrasound array: a simulation workflow *IEEE Trans. Radiat. Plasma Med. Sci.* **7** 83–95
Sulak L et al 1979 Experimental studies of the acoustic signature of proton beams traversing fluid media *Nucl. Instrum. Methods* **161** 203–17
Sundaram J, Mellein B R and Mitragotri S 2003 An experimental and theoretical analysis of ultrasound-induced permeabilization of cell membranes *Biophys. J.* **84** 3087–101
Toulemonde M, Surdutovich E and Solov'yov A V 2009 Temperature and pressure spikes in ion-beam cancer therapy *Phys. Rev.* E **80** 031913
Treeby B E and Cox B T 2010 k-wave: MATLAB toolbox for the simulation and reconstruction of photoacoustic wave fields *J. Biomed. Opt.* **15** 021314
Vozenin M-C et al 2019 The advantage of FLASH radiotherapy confirmed in mini-pig and cat-cancer patients *Clin. Cancer Res.* **25** 35–42
Webster D, Pond J, Dyson M and Harvey W 1978 The role of cavitation in the *in vitro* stimulation of protein synthesis in human fibroblasts by ultrasound *Ultrasound Med. Biol.* **4** 343–51
Yu Y, Li Z, Zhang D, Xing L and Peng H 2019 Simulation studies of time reversal-based protoacoustic reconstruction for range and dose verification in proton therapy *Med. Phys.* **46** 3649–62